

Journal of Materials Chemistry A

Accepted Manuscript



This is an *Accepted Manuscript*, which has been through the Royal Society of Chemistry peer review process and has been accepted for publication.

Accepted Manuscripts are published online shortly after acceptance, before technical editing, formatting and proof reading. Using this free service, authors can make their results available to the community, in citable form, before we publish the edited article. We will replace this *Accepted Manuscript* with the edited and formatted *Advance Article* as soon as it is available.

You can find more information about *Accepted Manuscripts* in the [Information for Authors](#).

Please note that technical editing may introduce minor changes to the text and/or graphics, which may alter content. The journal's standard [Terms & Conditions](#) and the [Ethical guidelines](#) still apply. In no event shall the Royal Society of Chemistry be held responsible for any errors or omissions in this *Accepted Manuscript* or any consequences arising from the use of any information it contains.

**Kinetic Molecular Sieving, Thermodynamic and Structural Aspects of Gas/Vapor
Sorption on Metal Organic Framework**

$[\text{Ni}_{1.5}(\text{4,4}'\text{-bipyridine})_{1.5}(\text{H}_3\text{L})(\text{H}_2\text{O})_3][\text{H}_2\text{O}]_7$ where $\text{H}_6\text{L} =$

2,4,6-trimethylbenzene-1,3,5-triyl tris(methylene) triphosphonic acid.

Xuebo Zhao¹, Jon G. Bell², Si-fu Tang³, Liangjun Li¹ and K Mark Thomas²

¹Research Institute of Unconventional Petroleum and Renewable Energy, China

University of Petroleum (East China), Qingdao 266580, P. R. China

²Wolfson Northern Carbon Reduction Laboratories, School of Chemical Engineering

and Advanced Materials, Newcastle University, Newcastle upon Tyne, NE1 7RU,

U.K.

³Key Laboratory of Biofuel, Chinese Academy of Sciences, Qingdao Institute of

Bioenergy and Bioprocess Technology, Qingdao, Shandong 266101, P. R. China

Abstract:

A metal organic framework $[\text{Ni}_{1.5}(\text{4,4}'\text{-bipy})_{1.5}(\text{H}_3\text{L})(\text{H}_2\text{O})_3] \cdot [\text{H}_2\text{O}]_7$ where $\text{H}_6\text{L} = 2,4,6\text{-trimethylbenzene-1,3,5-triyl tris(methylene) triphosphonic acid}$ and $\text{4,4}'\text{-bipy} = 4,4'\text{-bipyridine}$ has been prepared. The structures of $[\text{Ni}_{1.5}(\text{4,4}'\text{-bipy})_{1.5}(\text{H}_3\text{L})(\text{H}_2\text{O})_3] \cdot [\text{H}_2\text{O}]_7$ and the desolvated form $[\text{Ni}_{1.5}(\text{4,4}'\text{-bipy})_{1.5}(\text{H}_3\text{L})(\text{H}_2\text{O})_3]$ have been determined by single crystal X-ray diffraction and the framework structures are virtually identical with the former having disordered water molecules in the pores. The framework structure comprise of two-dimensional $\text{Ni}_{1.5}(\text{H}_3\text{L})$ layers and $\text{4,4}'\text{-bipy}$ linkers acting as pillars with an unusual framework topology of a (3, 3, 6) net that can be denoted as: $\{4.6^2\}_2\{6^3\}_2\{6^8.8^5.10^2\}$. The framework has one-dimensional channels decorated with acidic O-H groups with irregular shape varying from narrow windows (cross section: $4.2 \times 4.2 \text{ \AA}$) to pore cavities (diameter: $\sim 12 \text{ \AA}$). Thermogravimetric studies showed that both coordinated and lattice water molecules adsorbed in pores were removed in ultra-high vacuum to give $[\text{Ni}_{1.5}(\text{4,4}'\text{-bipy})_{1.5}(\text{H}_3\text{L})]$. The water vapor adsorption isotherm for $[\text{Ni}_{1.5}(\text{4,4}'\text{-bipy})_{1.5}(\text{H}_3\text{L})]$ showed that 3 coordinated and ~ 7 pore lattice water molecules were adsorbed and the framework structure was reformed. The desorption isotherm showed that the lattice water was easily desorbed in vacuum at 20°C to form $[\text{Ni}_{1.5}(\text{4,4}'\text{-bipy})_{1.5}(\text{H}_3\text{L})(\text{H}_2\text{O})_3]$. The ethanol adsorption isotherms for $[\text{Ni}_{1.5}(\text{4,4}'\text{-bipy})_{1.5}(\text{H}_3\text{L})]$ for temperature range $20\text{-}50^\circ\text{C}$ were markedly hysteretic. The stoichiometry was $[\text{Ni}_{1.5}(\text{4,4}'\text{-bipy})_{1.5}(\text{H}_3\text{L})] \cdot [1.11\text{C}_2\text{H}_5\text{OH}]$ at $p/p^0 = 0.97$ and 20°C gave a total pore volume approximately half that of

$[\text{Ni}_{1.5}(\text{4,4}'\text{-bipy})_{1.5}(\text{H}_3\text{L})(\text{H}_2\text{O})_3]$. The desorption isotherms show that ethanol is strongly retained with decreasing pressure indicating a stable framework structure. The kinetic profiles for oxygen, nitrogen, carbon dioxide, and water and ethanol vapors, can be described by Fickian, combined barrier resistance/diffusion (CBRD), and stretched exponential models for both adsorption and desorption. Gas adsorption studies for $[\text{Ni}_{1.5}(\text{4,4}'\text{-bipy})_{1.5}(\text{H}_3\text{L})]$ reveal kinetic molecular sieving occurs with very high kinetic selectivity for O_2/N_2 at 0°C . Carbon dioxide adsorption has intermediate rates of adsorption between oxygen and nitrogen. The isosteric enthalpy for CO_2 adsorption at zero surface coverage was $30.7 \pm 2.4 \text{ kJ mol}^{-1}$. The corresponding activation energy for diffusion of CO_2 into the framework was $\sim 48 \text{ kJ mol}^{-1}$. Narrow constrictions in the porous structure of $[\text{Ni}_{1.5}(\text{4,4}'\text{-bipy})_{1.5}(\text{H}_3\text{L})]$ give rise to kinetic molecular sieving effects and do not allow adsorption of molecules such as methane, which has a larger cross-section. The selectivity for CO_2/CH_4 was very high (x 1000) at 30°C . The adsorption results are discussed in terms of diffusion, thermodynamics and surface interactions in pores.

1. INTRODUCTION

Adsorption methods are widely used in gas separation processes and for the removal of trace amounts of contaminant species from gas streams. Industrial applications¹ include air separation², carbon dioxide removal from flue gases^{3, 4}, volatile organic compound (VOC) capture^{5, 6}, desulfurization of natural gas⁷ etc. There is considerable current research interest in the use and development of new porous materials for gas storage, separation and purification for a variety of applications. Newly developed types of porous materials including metal organic frameworks (MOFs), porous polymers etc. often have unique additional characteristics such as framework flexibility, which may have advantages in specific applications compared with activated carbons and zeolites. Porous MOFs may have additional interesting characteristics such as magnetism^{8, 9}, luminescence¹⁰ etc. and other potential applications in catalysts^{11, 12}, sensors¹³ etc. There has been considerable emphasis on the synthesis of MOFs with large pores for use in gas storage applications. However, in the case of gas separation, frameworks with narrow in constrictions pores are necessary in order to distinguish between molecules by kinetic mechanisms or with surface chemistry to enhance interactions with target species.

A wide range of MOFs have been prepared mainly from multidentate carboxylate, azole, and pyridinic ligands with first row transition metals. Micropores can be tuned systematically to select molecules on the basis of size using both kinetic and size exclusion processes and functional group sites, which may have different specific

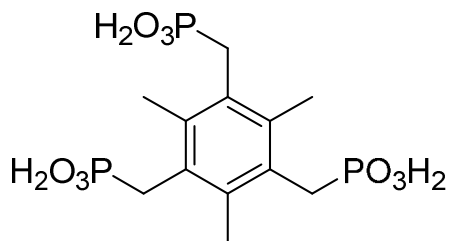
interactions with gases/vapors for the recognition and separation of small molecules. Microporous MOFs have predictable structures pre-determined by the coordination geometries of the secondary building units (SBUs) and the pore size may be systematically varied by changing the organic bridging pillars/linkers. SBUs and organic moieties may provide open metal sites and the Lewis basic/acidic sites for specific interactions with small molecules.

Phosphonate MOFs are considerably rarer than MOFs with carboxylate linkers, with phosphonates forming stronger bonds to metals than carboxylate groups.^{14, 15} The high thermal stability and low solubility are desirable features of the phosphonate MOFs. However, unlike carboxylate ligands, phosphonates do not form SBUs with metal ions, making it difficult to design porous phosphonate materials. Phosphonate groups have 3 oxygen atoms capable of coordinating to metals, can coordinate in varying states of protonation and have a wide variety of coordination modes to metals.¹⁴ The possibility of coordination of two phosphonate oxygen atoms coordinating to a metal leaving P-OH surface groups gives an acidic surface. A limited number of highly crystalline MOFs with phosphonate ligands are known, but poorly crystalline materials with high thermal and chemical stability also exist.¹⁴ The phosphonate MOFs can be categorized according to the ligand as follows¹⁴ 1) alkyl phosphonates¹⁶⁻¹⁹, 2) piperazinylphosphonates²⁰⁻²⁴ and 3) arylphosphonates.²⁵⁻³⁰ These porous materials include materials with a range of pore size, framework flexibility and interesting surface chemistry. Recently phosphonate MOFs have been shown to have high proton conducting characteristics.³¹⁻³⁴

In this study the synthesis and structures of $[\text{Ni}_{1.5}(\text{4,4}'\text{-bipy})_{1.5}(\text{H}_3\text{L})(\text{H}_2\text{O})_3] \cdot [\text{H}_2\text{O}]_7$ and the desolvated form $[\text{Ni}_{1.5}(\text{4,4}'\text{-bipy})_{1.5}(\text{H}_3\text{L})(\text{H}_2\text{O})_3]$ where $\text{H}_6\text{L} =$ 2,4,6-trimethylbenzene-1,3,5-triyl *tris*(methylene) triphosphonic acid, which include 4,4' bipyridine as structural pillars, have been investigated. The reformation of frameworks $[\text{Ni}_{1.5}(\text{4,4}'\text{-bipy})_{1.5}(\text{H}_3\text{L})(\text{H}_2\text{O})_3] \cdot [\text{H}_2\text{O}]_7$ and $[\text{Ni}_{1.5}(\text{4,4}'\text{-bipy})_{1.5}(\text{H}_3\text{L})(\text{H}_2\text{O})_3] \cdot [\text{H}_2\text{O}]_3$ from $[\text{Ni}_{1.5}(\text{4,4}'\text{-bipy})_{1.5}(\text{H}_3\text{L})]$ during water vapor adsorption/desorption was investigated. The adsorption of ethanol on $[\text{Ni}_{1.5}(\text{4,4}'\text{-bipy})_{1.5}(\text{H}_3\text{L})]$ to form a new framework was studied. The objective of this study was to investigate the link between structure and function through framework structural change with adsorption thermodynamic and kinetic characteristics. The role of kinetic molecular sieving of oxygen, nitrogen and carbon dioxide through windows in the pore structure are compared with thermodynamic characteristics of the completely desolvated MOF $[\text{Ni}_{1.5}(\text{4,4}'\text{-bipy})_{1.5}(\text{H}_3\text{L})]$.

2. EXPERIMENTAL SECTION

2.1 Materials and Synthesis. All starting chemicals were obtained from commercial sources and used without further purification. The synthesis of 2,4,6-trimethylbenzene-1,3,5-triyl *tris*(methylene)triphosphonic acid (H_6L) (see Scheme 1) was carried out using the literature method (see supporting information, Figures S1 and S2).^{35, 36}



Scheme 1 Ligand (2,4,6-trimethylbenzene-1,3,5-triyl) *tris*(methylene)triphosphonic acid

2.1.2 Synthesis of $[\text{Ni}_{1.5}(\text{4,4}'\text{-bipy})_{1.5}(\text{H}_3\text{L})(\text{H}_2\text{O})_3] \cdot [\text{H}_2\text{O}]_7$

2,4,6-trimethylbenzene-1,3,5-triyl *tris*(methylene)triphosphonic acid (H_6L , 0.2011 g, 0.5 mmol), $\text{NiSO}_4 \cdot 6\text{H}_2\text{O}$ (0.1971 g, 0.75 mmol), 4,4'-bipy (0.1171 g, 0.75 mmol) ($\text{H}_6\text{L}:\text{Ni}:4,4'\text{-bipy} = 1:1.5:1.5$) and 10 mL water were placed in a Teflon-lined autoclave and stirred for 30 minutes. Experiments in the temperature range 120-160 °C showed that the pH values before and after the reaction were approximately 4 and 3, respectively. The optimum conditions for maximizing the yield of crystals with well-defined shape/size were as follows. The reaction mixture was heated at 140 °C for 4 days and cooled to room temperature over a period of 24 hours at a rate of about 4 °C h⁻¹. After washing with deionized water, blue crystals with well-defined shape (see Supporting Information, Figure S3) were isolated in high yield (about 81% based on Ni). The material readily loses water located in the porous structure as shown by thermogravimetric and water desorption measurements and this influences the chemical analysis *vide infra*. Elemental analysis (%) calcd for $[\text{Ni}_{1.5}(\text{4,4}'\text{-bipy})_{1.5}(\text{H}_3\text{L})(\text{H}_2\text{O})_3][\text{H}_2\text{O}]_7$ ($\text{C}_{27}\text{H}_{50}\text{N}_3\text{Ni}_{1.5}\text{O}_{19}\text{P}_3$): C 35.97, H 5.59, N 4.66; found: C 36.51, H 5.60, N 4.72. IR(KBr, cm⁻¹): 3417(s, br), 2923(m), 2390(w), 1609(s), 1537(w), 1492(w), 1417(m), 1287(w), 1259(w), 1221(m), 1173(s), 1141(s),

1069(m, sh), 1046(s, sh), 1023(vs), 930(s), 825(w), 813(m), 757 (w), 728(w), 693(w), 635(m), 558(w), 493(m) (see Figure S8).

2.2 Characterization Methods Used

Elemental analyses were performed on a Vario EL III elemental analyzer. IR spectra were recorded on a Nicolet 6700 FTIR Spectrometer in the range of 4000-400 cm^{-1} using KBr pellets. Thermogravimetric analysis (TGA) was carried out on a NETZSCH STA 449C unit at a heating rate of 10 $^{\circ}\text{C min}^{-1}$ under a nitrogen atmosphere. SEM micrographs were taken on a HITACHI S-4800 scanning electron microscope with an accelerating voltage of 3 kV. ^1H NMR spectra were recorded on a Bruker AVANCE-III NMR (600 MHz).

2.2.1 Powder X-ray Diffraction (PXRD). Powder X-ray diffraction profiles were obtained on a D8 Advance diffractometer using CuK_{α} radiation. The activated powder sample was obtained by loading the ‘as-synthesized’ sample in a capillary (diameter: 0.5 mm) and drying at 110 $^{\circ}\text{C}$ for 6 hours under dynamic vacuum at 1 mbar pressure. Three activated additional powder samples were also investigated to test their crystallinity and thermal stability (Figure 3). The respective activation conditions are: 1) drying the ‘as-synthesized’ sample in a vacuum oven for 6 hours at 110 $^{\circ}\text{C}$; 2) drying the ‘as-synthesized’ sample in a capillary (diameter: 0.5mm) at 105 $^{\circ}\text{C}$ for 12 hours under 10^{-7} mbar and 3) drying the ‘as-synthesized’ sample in a vacuum oven for 6 hours at 240 $^{\circ}\text{C}$.

2.2.2 Single-Crystal Structure Determination. Single crystal X-ray diffraction measurements of the ‘as-synthesized’ $[\text{Ni}_{1.5}(\text{4,4'}\text{-bipy})_{1.5}(\text{H}_3\text{L})(\text{H}_2\text{O})_3]\cdot[\text{H}_2\text{O}]_7$ and

activated $[\text{Ni}_{1.5}(\text{4,4}'\text{-bipy})_{1.5}(\text{H}_3\text{L})(\text{H}_2\text{O})_3]$ heated to 110°C at atmospheric pressure were carried out on a Bruker SMART APEX II CCD diffractometer (Mo $K\alpha$ radiation, $\lambda = 0.71073 \text{ \AA}$) at room temperature. The SAINT software was used for integration of intensity of reflections and scaling.³⁷ Numerical absorption corrections were carried out with the program SADABS.³⁸ Crystal structures were solved by direct methods using the SHELXS program.³⁹ Subsequent difference Fourier analyses and least squares refinement with SHELXTL-97⁴⁰ allowed for the location of the atom positions. In the final step of the crystal structure refinement hydrogen atoms of idealized $-\text{CH}_2$ and $-\text{CH}_3$ groups were added and treated with the riding atom mode; their isotropic displacement factors were chosen as 1.2 and 1.5 times the preceding carbon atom, respectively. In the triphosphonate ligand, one $-\text{CPO}_3\text{H}$ group (C5, P1, O1, O2, O3) and one methyl group (C8) lie on a mirror plane. The hydrogen atoms on the lattice water molecules were not located, but included in the formula. Most guest water molecules in the channels of both the 'as-synthesized' and partly activated materials were disordered and could not be modeled. Hence, their electron density peaks were removed by the SQUEEZE implemented in PLATON.⁴¹ The amounts of water present were determined by thermogravimetric, water adsorption results and elemental analyses. The crystal data and structure refinement results are listed in Table 1 and bond lengths are given in Table S1 in the Supporting Information.

Table 1. Crystallographic Details for ‘As-synthesized’

[Ni_{1.5}(4,4'-bipy)_{1.5}(H₃L)(H₂O)₃]·[H₂O]₇ and Sample Activated at 110°C in Vacuum.

Compound	[Ni _{1.5} (4,4'-bipy) _{1.5} (H ₃ L)(H ₂ O) ₃]·[H ₂ O] ₇	Sample Activated at 110°C
Formula	C ₂₇ H ₃₇ N ₃ Ni _{1.5} O _{12.5} P ₃	C ₂₇ H _{36.5} N ₃ Ni _{1.5} O _{12.25} P ₃
fw	784.57	780.06
space group	I-42m	I-42m
<i>a</i> (Å)	18.5564(16)	18.5126(12)
<i>b</i> (Å)	18.5564(16)	18.5126(12)
<i>c</i> (Å)	22.937(4)	22.922(3)
<i>α</i> (deg)	90	90
<i>β</i> (deg)	90	90
<i>γ</i> (deg)	90	90
<i>V</i> (Å ³)	7898.0(17)	7855.6(37)
<i>Z</i>	8	8
<i>D</i> _{calcd.} (g cm ⁻³)	1.320	1.319
abs coeff (mm ⁻¹)	0.900	0.904
reflns collected	31610	14603
independent	3641/ 0.1509	4622/ 0.0559
reflns/ <i>R</i> _{int}		
GOF on <i>F</i> ²	1.018	0.857
final <i>R</i> indices	0.0864, 0.1983	0.0585, 0.1313
[<i>I</i> >2σ(<i>I</i>): <i>R</i> ₁ , <i>wR</i> ₂		
<i>R</i> indices (all data):	0.1409, 0.2281	0.1179, 0.1468
<i>R</i> ₁ , <i>wR</i> ₂		

$$^a R_1 = \sum ||F_o| - |F_c|/\sum |F_o||; wR_2 = \{\sum w(F_o^2 - F_c^2)^2/\sum w(F_o^2)^2\}^{1/2}.$$

Crystallographic F.W = [Ni_{1.5}(4,4'-bipy)_{1.5}(H₃L) (H₂O)₃]

2.3 Gas Adsorption Measurements

Adsorption characteristics of oxygen, nitrogen and carbon dioxide, and water and ethanol vapors on the porous metal organic phosphonate framework material were investigated using an Intelligent Gravimetric Analyzer (IGA), supplied by Hiden Isochema Ltd., Warrington, UK. The instrument is an ultra-high vacuum (UHV) system comprising of a fully computer controlled microbalance with pressure and temperature regulation systems. The microbalance has a long-term stability of $\pm 1 \mu\text{g}$ with a weighing resolution of $0.2 \mu\text{g}$. The adsorbent sample ($50 \pm 1 \text{ mg}$) was outgassed to a constant weight, at $< 10^{-6} \text{ Pa}$, at 110°C . The weight loss was monitored throughout the outgas period and the weight loss of 19.74 wt% was consistent with the loss of both coordinated and lattice water molecules in pores (See Figure S9 Supporting Information for thermogravimetric profile). The pressure transducers had individual ranges of 0-0.2 kPa, 0-10 kPa and 0-100 kPa. The pressure set point accuracy was 0.02 % of the range employed. The sample temperature was recorded using a thermocouple located $\sim 5 \text{ mm}$ from the sample. The equilibrium uptake value was determined as being 99 % of the predicted value, calculated in real time using the mass uptake profile. Saturated vapor pressures for H_2O adsorption were calculated using the Antoine equation:

$$\log(p^0) = A - \frac{B}{T + C} \quad (1)$$

where p^0 is the saturated vapor pressure (Torr), T is the temperature (K), and A, B, and C are adsorbate dependent constants. The parameters used for water vapor for range -5 to 110°C were $A=8.09553$, $B=1747.32$ and $C=235.074$.

Saturated vapor pressures for carbon dioxide and ethanol were calculated five-parameter equation⁴² as described below:

$$\log(p^0) = A - B/T + C \log T + DT + ET^2 \quad (2)$$

The parameters used were as follows, CO₂ ((-90 to 31°C) where $A=35.0169$, $B=-1511.9$, $C=-11.334$, $D=9.3368 \times 10^{-3}$, $E=1.7136 \times 10^{-9}$) and ethanol vapor ((-114 to 243°C) where $A=23.8442$, $B=-2864.2$, $C=-5.0474$, $D=3.7448 \times 10^{-11}$, $E=2.7361 \times 10^{-7}$)

3. RESULTS AND DISCUSSION

3.1 Structure of compound [Ni_{1.5}(4,4'-bipy)_{1.5}(H₃L)(H₂O)₃]·[H₂O]₇

The single-crystal X-ray diffraction measurement revealed that compound [Ni_{1.5}(4,4'-bipy)_{1.5}(H₃L)(H₂O)₃]·[H₂O]₇ crystallized in the tetragonal *I*-42m space group (No. 121). In each asymmetric unit, there are three quarters of crystallographically distinct Ni atoms (Ni1 25%; Ni2 50%), half triply-deprotonated (H₃L)³⁻ ligand, three quarters of 4,4'-bipy, one and a half coordinated aqua ligands (O1w, O2w 50%) and one quarter of lattice water molecules (O3w 12.5 %, O4w 12.5 %), corresponding to the molecular formula of [Ni_{1.5}(4,4'-bipy)_{1.5}(H₃L)(H₂O)₃]·[H₂O]_{0.75}. The three -CH₂PO₃ arms in the triphosphonate ligand adopt a *trans* geometry (see Figure 1a). Each phosphoric acid group is single deprotonated and links to one nickel ion with monodentate coordination (either Ni1 or Ni2). Both Ni1 and Ni2 have octahedral coordination, but

have different coordination spheres. For Ni1, it is coordinated by four oxygen atoms (O4, O4#1, O4#2 and O4#3; operators: #1 $-x+1, -y, z$; #2 $y+1/2, -x+1/2, -z+1/2$; #3 $-y+1/2, x-1/2, -z+1/2$) of four triphosphonate ligands at the equatorial positions (Ni1-O4: 2.078(5) Å) and two nitrogen atoms (N1 and N1#2) from two 4,4'-bipy molecules at the axis positions (Ni1-N1: 2.169(11) Å). For Ni2, the coordination sphere is completed by one oxygen atom (O1, Ni2-O1: 1.989(18) Å) from one triphosphonate ligand, two nitrogen atoms (N2 and N2#4; operator: #4 $-y+1, -x+1, z$; Ni2-N2: 2.099(10) Å) from two 4,4'-bipy molecules and three aqua ligands (O1w, O1w #4 and O2w; Ni2-O1w: 2.109(8); Ni2-O2w: 2.069(11) Å) (See supporting information, Table S1).

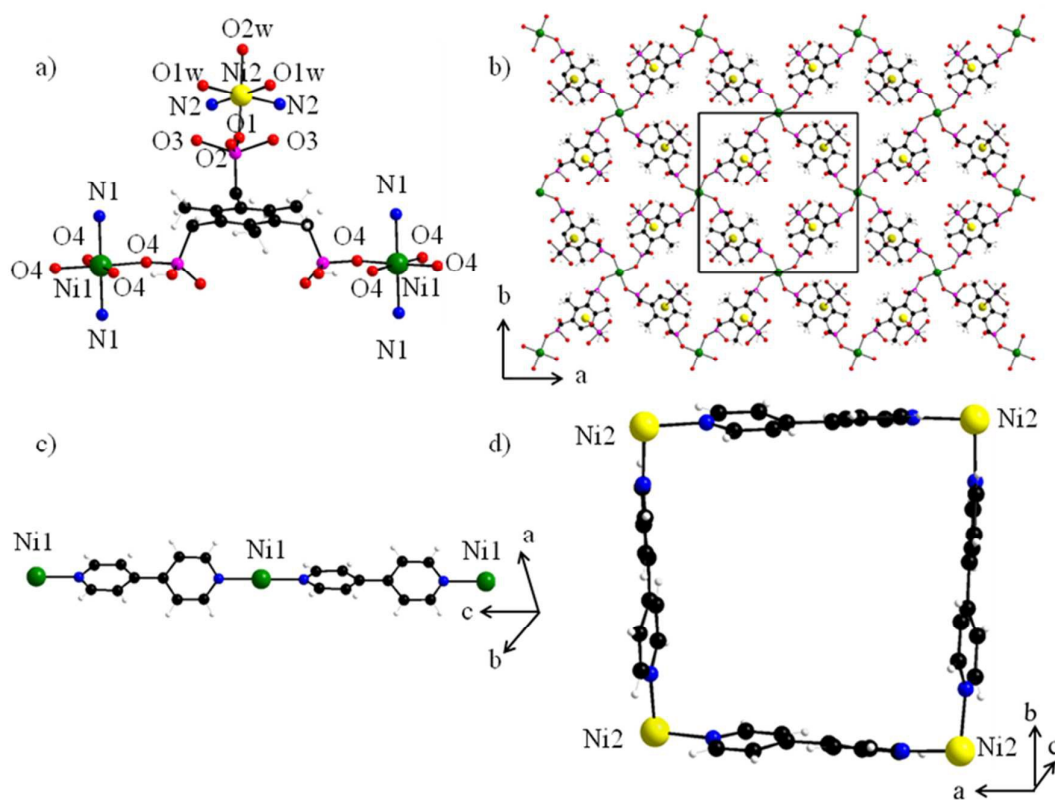


Figure 1. Crystal structure of $[\text{Ni}_{1.5}(\text{4,4}'\text{-bipy})_{1.5}(\text{H}_3\text{L})(\text{H}_2\text{O})_3] \cdot [\text{H}_2\text{O}]_7$ (a) Coordination environment of the phosphonate ligand; (b) 2D layer in the ab -plane; (c)

1D $[\text{Ni}(4,4'\text{-bipy})]_{\infty}$ chain along c -axis; (d) $[\text{Ni}(4,4'\text{-bipy})]_4$ distorted circle. Ni1, Ni2, C, N, P, and O atoms are drawn as green, yellow, black, blue, purple, and red balls, respectively.

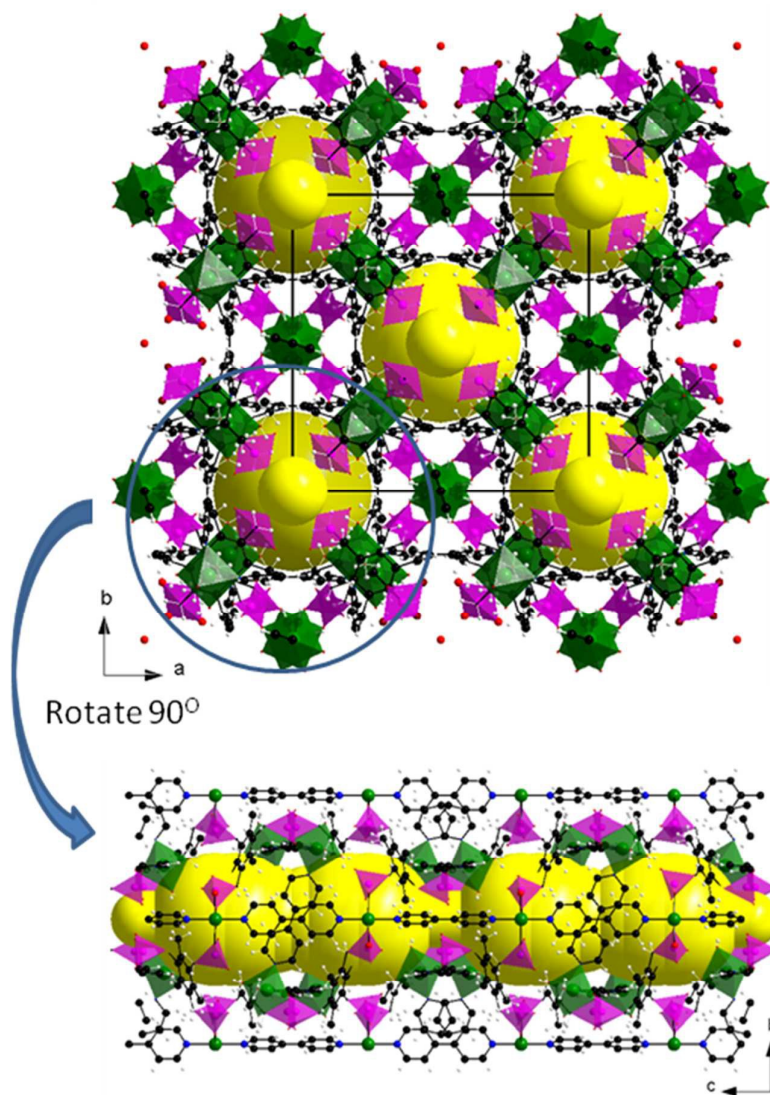


Figure 2. View of the structure of $[\text{Ni}_{1.5}(4,4'\text{-bipy})_{1.5}(\text{H}_3\text{L})(\text{H}_2\text{O})_3] \cdot [\text{H}_2\text{O}]_7$ down the c -axis (top); 1D channel along c -axis (bottom). Cavities and windows are drawn as yellow balls and sticks, respectively. The $-\text{CPO}_3$ tetrahedra and NiO_4N_2 octahedra are shaded in purple and green, respectively. Ni, C, N, P, and O atoms are drawn as green, black, blue, purple, and red balls, respectively.

The whole structure can be envisaged as comprising of two dimensional $\text{Ni}_{1.5}(\text{H}_3\text{L})$ layers and 4,4'-bipy linkers acting as pillars (see Figure 1). The tritopic H_3L^{3-} ligands link with Ni1 ions using its two $-\text{PO}_3\text{H}$ groups and generate 2D square-grid-like layers in the ab plane with the third one (binding with Ni2) tethering above alternative sides of the central aromatic core. These layers are further pillared at the Ni1 position (0.5, 0, 0.25) along the c axis and bridged at the Ni2 position of neighboring layers by 4,4'-bipy linkers to generate a 3D framework (see Figure 2) with 1D channels running along the c axis which are braced by the 1D infinite $[\text{Ni1}(4,4'\text{-bipy})]_{\infty}$ chains and confined by the $[\text{Ni2}(4,4'\text{-bipy})]_4$ circles (diameter: about 10.7 Å). The channels are different from the straight-through passage observed for some known MOFs, for example, the 1D channel in compound $[\text{Ni}_{1.5}(4,4'\text{-bipy})_{1.5}(\text{H}_3\text{L})(\text{H}_2\text{O})_3] \cdot [\text{H}_2\text{O}]_7$ has $-\text{CH}_2\text{PO}_3$ groups (C5, P1, O1, O2, O3) protruding in the channel to form small windows. Therefore, the channels found in compound $[\text{Ni}_{1.5}(4,4'\text{-bipy})_{1.5}(\text{H}_3\text{L})(\text{H}_2\text{O})_3] \cdot [\text{H}_2\text{O}]_7$ can be seen as being constructed from a succession of narrow pore cavities (diameter: about 12 Å) and windows (cross section: 4.2×4.2 Å) (see Figure 2).

Alternatively, the structure can also be described as being constructed from bridging tridentate triphosphonate ligands, 1D infinite $[\text{Ni1}(4,4'\text{-bipy})]$ chains and distorted $[\text{Ni2}(4,4'\text{-bipy})]_4$ circles (see Figure S5). Ni1 forms 1D chains along c -axis with 4,4'-bipy, whereas Ni2 forms $[\text{Ni2}(4,4'\text{-bipy})]_4$ circles with 4,4'-bipy. The flexible tritopic phosphonate ligands bridge these circles and chains into a 3D framework.

3.2 Activation of $[\text{Ni}_{1.5}(\text{4,4}'\text{-bipy})_{1.5}(\text{H}_3\text{L})(\text{H}_2\text{O})_3] \cdot [\text{H}_2\text{O}]_7$

The TGA profile for $[\text{Ni}_{1.5}(\text{4,4}'\text{-bipy})_{1.5}(\text{H}_3\text{L})(\text{H}_2\text{O})_3] \cdot [\text{H}_2\text{O}]_7$ shows that there are four weight loss steps in the temperature range of 30-900 °C under a nitrogen atmosphere. The first step occurred in the range of 40-140 °C and this was followed by a step for temperature range 140-240 °C. These steps corresponded to the initial loss of 7 lattice water molecules from analytical data (calculated 13.99%; observed: 12.54%) and followed by 3 coordinated water molecules (calculated 19.99%; observed: 18.87%), respectively (See the supporting information, Figure S9). The lower observed weight loss values are attributed to loss of some pore lattice water during sample drying prior to thermogravimetric analysis. The activation of $[\text{Ni}_{1.5}(\text{4,4}'\text{-bipy})_{1.5}(\text{H}_3\text{L})(\text{H}_2\text{O})_3] \cdot [\text{H}_2\text{O}]_7$ with loss of coordinated water to form $[\text{Ni}_{1.5}(\text{4,4}'\text{-bipy})_{1.5}(\text{H}_3\text{L})]$ results in a change from green to yellow in color. At higher temperatures, the organic moiety started to decompose slowly. However, the activation of $[\text{Ni}_{1.5}(\text{4,4}'\text{-bipy})_{1.5}(\text{H}_3\text{L})(\text{H}_2\text{O})_3] \cdot [\text{H}_2\text{O}]_7$ was sensitive to both temperature and evacuation conditions. The loss of water from the $[\text{Ni}_{1.5}(\text{4,4}'\text{-bipy})_{1.5}(\text{H}_3\text{L})(\text{H}_2\text{O})_3] \cdot [\text{H}_2\text{O}]_7$ framework is slow at 22°C under ultra-high vacuum as confirmed by the water vapor desorption results *vide infra*. The structure of an activated phase obtained by drying the 'as-synthesized' sample of $[\text{Ni}_{1.5}(\text{4,4}'\text{-bipy})_{1.5}(\text{H}_3\text{L})(\text{H}_2\text{O})_3]$ under vacuum was also characterized for comparison. The results indicated that the overall connectivity of the framework was retained, only slight shrinkage was observed for the cell parameters. The crystallography data are consistent with the presence of some residual lattice water. The total potential solvent

volume estimated by PLATON changes slightly from 24.3 to 24.5%.

From the view of topology, the triphosphonate ligand and Ni₂ behave as 3-connected nodes, whereas Ni₁ is 6-connected. Therefore the topology of the framework is a (3, 3, 6) net and can be denoted as: {4.6²}₂{6³}₂{6⁸.8⁵.10²} which is previously unknown (See supporting information, Figure S5).

3.3 PXRD Profiles

The PXRD results showed good correlation between the simulated profiles from the single-crystal structure data, the experimental profiles for ‘as-synthesized’ and a sample activated at 110°C and ~1 mbar for 6 h, suggesting good purity for the ‘as-synthesized’ sample and the porous framework structure was maintained after activation (See Figure 3). Activation for longer periods under vacuum showed evidence for weaker profiles indicating possibly some loss of crystalline [Ni_{1.5}(4,4'-bipy)_{1.5}(H₃L)(H₂O)₃] and the presence of weak additional peaks. Activation in a vacuum oven at 240°C for 6 h showed the absence of crystalline framework material. The PXRD profile of a sample of [Ni_{1.5}(4,4'-bipy)_{1.5}(H₃L)] after use for carbon dioxide gas adsorption studies followed by exposure to water showed that the framework structure reformed (Supporting Information, Figure S7b).

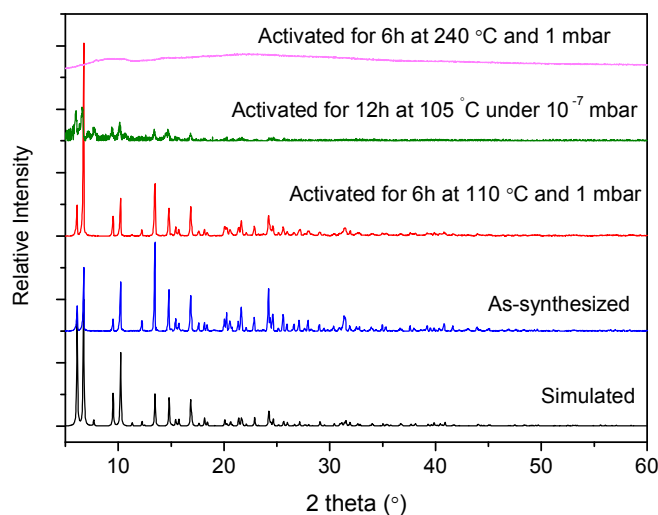


Figure 3. Comparison of PXRD profiles for $[\text{Ni}_{1.5}(\text{4,4}'\text{-bipy})_{1.5}(\text{H}_3\text{L})(\text{H}_2\text{O})_3]\cdot[\text{H}_2\text{O}]_7$ for various activation conditions

3.4 Gas adsorption characteristics

Characterization of the porous structure characteristics of the desolvated MOF is limited by the narrow windows in the structure, which give rise to activated diffusion effects. Nitrogen adsorption at -196°C was not appropriate for characterizing the pore structure because of activated diffusion effects resulting in kinetic limitations. Carbon dioxide adsorption studies for both -78 and 0°C showed that the adsorption kinetics were also very slow. Therefore, in order to characterize the porous structure of $[\text{Ni}_{1.5}(\text{4,4}'\text{-bipy})_{1.5}(\text{H}_3\text{L})]$, less conventional adsorption techniques were used.

3.4.1 Water Vapor Adsorption

The weight loss data from the *in-situ* activation of the MOF in ultrahigh vacuum resulted in loss of both coordinated and lattice water. Water vapor adsorption and desorption at 20°C were used to investigate the formation of the structure from the

activated sample $[\text{Ni}_{1.5}(4,4'\text{-bipy})_{1.5}(\text{H}_3\text{L})]$ and the subsequent desorption of water from the sample (See Figure 4a). The sample had an uptake $13.609 \text{ mmol g}^{-1}$ (24.517 mass\%) at $p/p^0 = 0.844$ corresponding to $[\text{Ni}_{1.5}(4,4'\text{-bipy})_{1.5}(\text{H}_3\text{L})(\text{H}_2\text{O})_3] \cdot [\text{H}_2\text{O}]_{6.82}$. Extrapolation of the isotherm to $p/p^0 = 1$ gave an uptake of $14.08 \text{ mmol g}^{-1}$ which corresponds to $7.1 \text{ H}_2\text{O}$ per $[\text{Ni}_{1.5}(4,4'\text{-bipy})_{1.5}(\text{H}_3\text{L})(\text{H}_2\text{O})_3]$. This is slightly lower than the $\sim 7.4 \text{ H}_2\text{O}$ per $[\text{Ni}_{1.5}(4,4'\text{-bipy})_{1.5}(\text{H}_3\text{L})(\text{H}_2\text{O})_3]$ expected based on the crystallographic Platon pore volume ($0.185 \text{ cm}^3 \text{ g}^{-1}$). Therefore, the formula $[\text{Ni}_{1.5}(4,4'\text{-bipy})_{1.5}(\text{H}_3\text{L})(\text{H}_2\text{O})_3] \cdot [\text{H}_2\text{O}]_7$ is used for the 'as-synthesized' framework. The adsorption/desorption isotherms are markedly hysteretic and the final desorption point was 4.19 mmol g^{-1} corresponding to retention of 3.02 molecules of H_2O , i.e. only coordinated water is retained. The adsorption/desorption isotherms imply that lattice water is readily lost under ambient conditions.

The water adsorption kinetics for $[\text{Ni}_{1.5}(4,4'\text{-bipy})_{1.5}(\text{H}_3\text{L})]$ at 20°C were slow as shown for pressure increment $0.05\text{-}0.1 \text{ mbar}$ in the Figure 4b which takes over 4h to equilibrate. Adsorption/desorption kinetics for porous materials can be described by several models including Linear Driving Force(LDF), Fickian, Stretched Exponential(SE) and Combined Barrier Resistance Diffusion (CBRD) models. The SE kinetic model is described by the following equation:

$$\frac{M_t}{M_e} = 1 - e^{-(kt)^\beta} \quad (3)$$

where M_t is the mass increase at time t during the adsorption following the pressure

increment, M_e is the equilibrium mass for pressure increment, k is the mass transfer kinetic parameter (s^{-1}) and t is the time (s). The exponent parameter (β) describes the distribution of relaxation times and depends on the porous material. The LDF model⁴³ has a single relaxation time and is a special case of the SE model when $\beta = 1$. The process is one-dimensional with a distribution of relaxation times when $\beta = 0.5$. The sample has a particle size distribution and the SE model does not require assumptions for particle shape/size.⁴⁴ The corresponding equation for desorption⁴⁵

$$\frac{M_t}{M_e} = e^{-(kt)^\beta} - 1 \quad (4)$$

At the start of desorption, $M_t = 0$ and at equilibrium, after completion of the desorption step, $M_e = M_t$ and $M_t/M_e = 1$

The SE model also provides good descriptions of Fickian diffusion into porous materials⁴⁴ and the related combined barrier resistance/diffusion models. The stretched exponential function is an approximation for uniformly convergent sums of exponentials.⁴⁶ The mathematical description for the Fickian diffusion model depends on the shape of the particles.⁴⁷ An average particle size/dimension has to be used in the equations and this is essentially a scaling factor.

Fick's law for isothermal diffusion into a homogeneous spherical particle is described by the following equation⁴⁷:

$$\frac{M_t}{M_e} = 1 - \frac{6}{\pi^2} \sum_{n=1}^{\infty} \left(\frac{1}{n^2} \right) \exp\left(\frac{-Dn^2\pi^2t}{r^2} \right) \quad (5)$$

where r is the particle radius and D is the diffusion coefficient.

The CBRD model assumes that a surface barrier resistance is present and

diffusion along pores in a spherical particle follows Fick's law. The equations for isothermal diffusion are as follows⁴⁸:

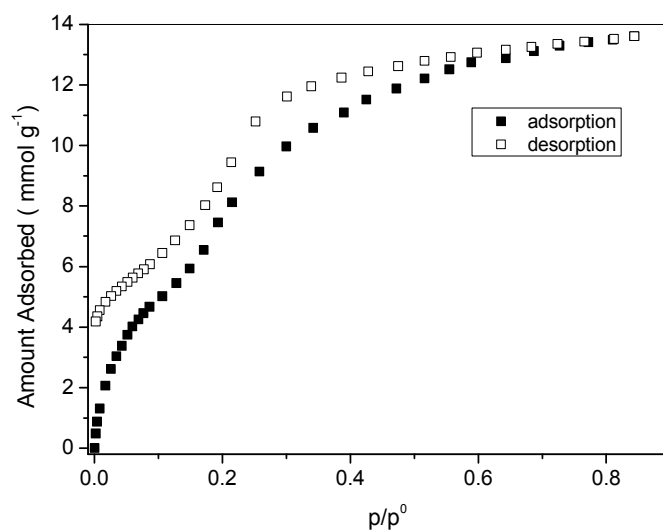
$$\frac{\partial C}{\partial t} = D \left[\left(\frac{\partial^2 C}{\partial r^2} \right) + \left(\frac{2}{r} \right) \left(\frac{\partial C}{\partial r} \right) \right] \quad (6)$$

where D is the crystallite diffusivity ($\text{m}^2 \text{s}^{-1}$), C is the sorbate concentration in the crystallite (mmol m^{-3}), r is the radial co-ordinate and t is the time.

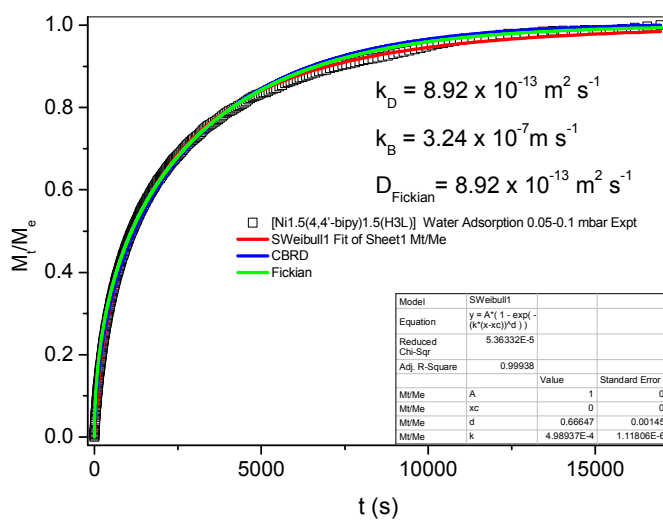
$$D \frac{\partial C(r_c, t)}{\partial r} = k_b (C^*(t) - C(r, t)) \quad (7)$$

where D is the crystallite diffusivity ($\text{m}^2 \text{s}^{-1}$), k_b is the surface barrier resistance (m s^{-1}), r is the radial co-ordinate, r_c is the radius of the crystallite (m), t is time(s), C is the sorbate concentration in the crystallite (mol m^{-3}) and C^* the surface concentration in equilibrium with the gas phase (mol m^{-3}). The boundary condition for adsorption for the differential equation is $C(r, 0) = 0$, which represents the concentration along the radial coordinate at time zero. The information derived from the model are the surface barrier parameter (k_b) and the diffusion coefficient for diffusion along the pores (k_d), which describe kinetic profiles intermediate between Fickian and LDF.⁴⁸

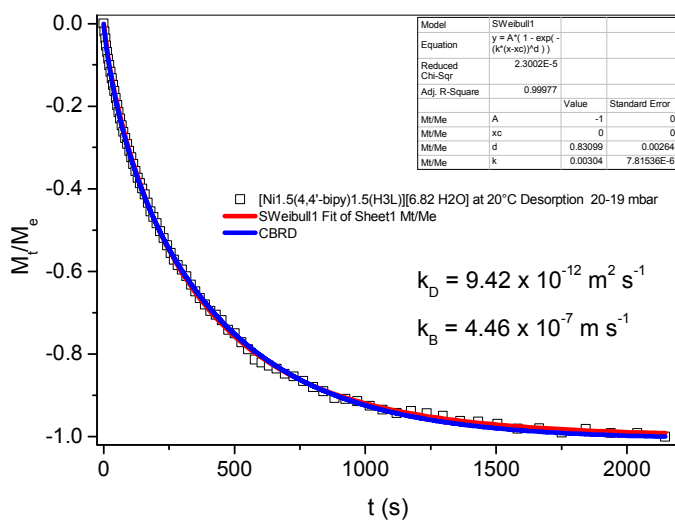
(a)



(b)



(c)



(d)

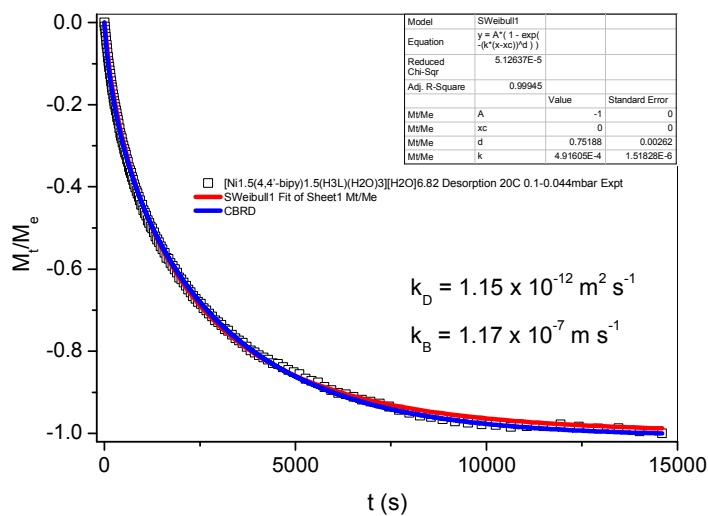


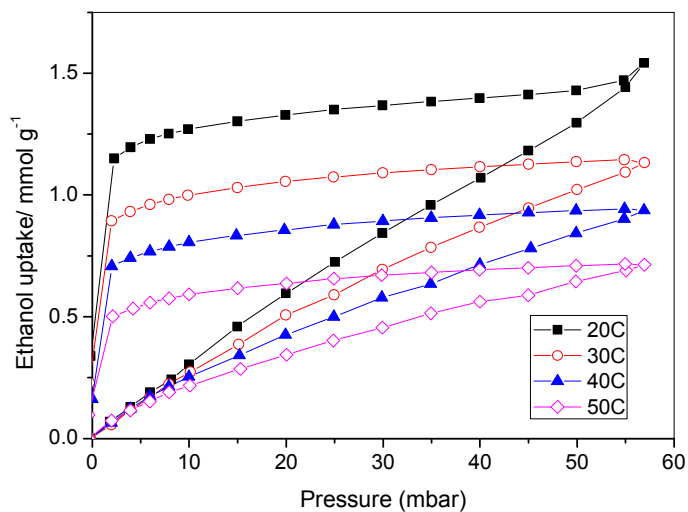
Figure 4. Water Vapor Adsorption/Desorption on [Ni_{1.5}(4,4'-bipy)_{1.5}(H₃L)] at 20°C (a) Adsorption/Desorption Isotherm, (b) Adsorption Kinetic Profile for Pressure Increment 0.05-0.1 mbar; (c) Desorption Kinetic Profile for Pressure Decrement

20-19 mbar and (d) Desorption Kinetic Profile for Pressure Decrement 0.1-0.044 mbar.

The adsorption kinetic profile in Figure 4b shows that all the Fickian, SE and CBRD models fit the profile. The SE exponent (β) parameter was 0.666 and this is consistent with Fickian diffusion. The Fickian model provides a good description and the CBRD model with an additional parameter does not provide a significant improvement. Therefore, the surface barrier is not significant under these experimental conditions and the adsorption kinetics are controlled by diffusion along the pores. Figures 4c and d show the water vapor desorption profiles at high uptake (pressure decrement 20-19 mbar) and also very low pressure (pressure decrement 0.1-0.044 mbar). It is apparent that overall the rate of adsorption decreases as the pressure decreases. However there is some variation in desorption rate with pressure which changes with chemical potential gradient reflected in the desorption isotherm. The desorption kinetic profiles slow on the steeper part of the isotherm where the surface barrier is rate determining (See Figure S10c, 6-5 mbar, $p/p^0 = 0.252-0.214$) and increase below $p/p^0 = 0.2$ before decreasing again to the equilibrated final desorption profile (see Figure 4d, and Supporting Information Figures S10d and e). The values of the Fickian Diffusion parameter (k_D) and barrier resistance kinetic parameter (k_B) were in the range $1-10 \times 10^{-12} \text{ m}^2 \text{ s}^{-1}$ and $4 - 60 \times 10^{-8} \text{ m s}^{-1}$, respectively.

3.4.2 Ethanol Vapor Adsorption

(a)



(b)

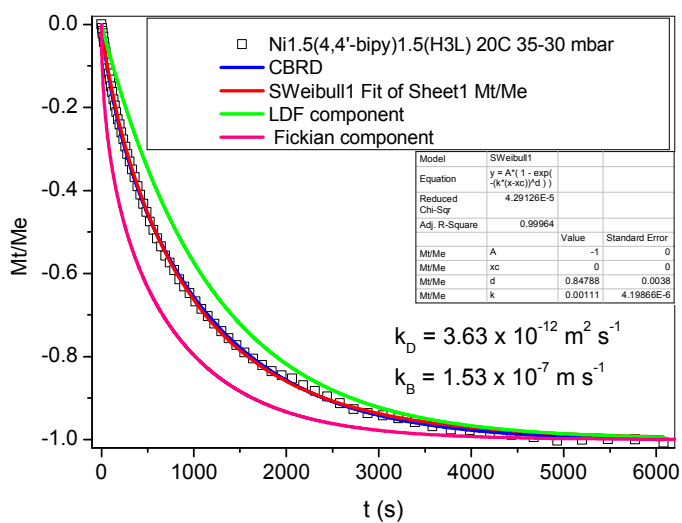


Figure 5. Adsorption/Desorption for Ethanol Adsorption on $[\text{Ni}_{1.5}(\text{4,4}'\text{-bipy})_{1.5}(\text{H3L})]$

(a) Isotherms in the Temperature Range 20-50°C, (b) Desorption Kinetic Profile

35-30 mbar decrement at 20°C and fitting to kinetic models.

The adsorption of ethanol vapor on the hydrophilic surface of $[\text{Ni}_{1.5}(\text{4,4}'\text{-bipy})_{1.5}(\text{H}_3\text{L})]$ was investigated to study the effect of introduction of hydrophobic character into the adsorbate on adsorption characteristics. The ethanol adsorption isotherms for $[\text{Ni}_{1.5}(\text{4,4}'\text{-bipy})_{1.5}(\text{H}_3\text{L})]$ are shown in Figure 5a. The adsorption isotherms are close to linearity, exhibit marked hysteresis and are markedly different from the water vapor isotherm in Figure 4a. The desorption isotherms (see Figure 5a) show that there is very strong retention of ethanol in the structure even at 50°C (ethanol Boiling Point = 78.4°C) suggesting a relatively stable framework structure is formed. The partial hydrophobic character in the ethanol has a marked effect on the isotherm shape. As expected, this is the reverse order to that observed for water and ethanol vapor adsorption on hydrophobic activated carbon surfaces.⁴⁹ The enthalpy of adsorption for ethanol on the two phases of $\text{Ni}_2(\text{4,4}'\text{-bipyridine})_3(\text{NO}_3)_4$ was in the range 40-58 kJ mol⁻¹.^{50, 51} The isosteric enthalpy (Q_{st}) for ethanol adsorption on $[\text{Ni}_{1.5}(\text{4,4}'\text{-bipy})_{1.5}(\text{H}_3\text{L})]$ was determined from graphs of $\ln(p)$ versus $1/T$ for specific amounts adsorbed and these graphs had good linearity (see Supporting Information, Figure S11a). The Q_{st} values increased with increasing uptake from 7.9 ± 1.7 kJ mol⁻¹ at 0.2 mmol g⁻¹ to 19.2 ± 0.6 kJ mol⁻¹ at 0.7 mmol g⁻¹ (see Figure S11b). This is lower than the enthalpy of vaporization for ethanol of 38.6 kJ mol⁻¹.⁵² The low value is probably due to framework structural change during adsorption. The ethanol uptake on $[\text{Ni}_{1.5}(\text{4,4}'\text{-bipy})_{1.5}(\text{H}_3\text{L})]$ at $p/p^0 = 0.97$ was 1.542 mmol g⁻¹ which corresponds to pore volume of 0.09 cm³ g⁻¹ assuming a density of 0.7893 g cm⁻³ for adsorbed ethanol. This value is approximately half the pore volume determined from water vapor

adsorption. This maximum ethanol uptake gives a stoichiometry of $[\text{Ni}_{1.5}(\text{4,4}'\text{-bipy})_{1.5}(\text{H}_3\text{L})]\cdot[1.11\text{C}_2\text{H}_5\text{OH}]$. The desorption from 57 to 49.9 mbar reduces the uptake to 1.43 mmol g^{-1} ($1.03 \text{ C}_2\text{H}_5\text{OH}$ per F.U.), while at 9.9 mbar the uptake was 1.27 mmol g^{-1} ($0.92 \text{ C}_2\text{H}_5\text{OH}$ per F.U.). The decrease in rates of desorption as the isotherm plateau is reached is shown in Figure S16e. The uptakes achieved at the maximum vapor pressure used of 57 mbar at 30, 40 and 50°C were correspondingly lower due to the lower relative pressure. This shows the effect of ethanol loading on the $[\text{Ni}_{1.5}(\text{4,4}'\text{-bipy})_{1.5}(\text{H}_3\text{L})]\cdot[\text{C}_2\text{H}_5\text{OH}]_x$ structure for uptakes down to 0.5 mmol g^{-1} ($0.36 \text{ C}_2\text{H}_5\text{OH}$ per F.U.) at 2 mbar and 50°C . However, similar hysteresis occurs at all temperatures studied ($20\text{-}50^\circ\text{C}$) and loadings suggesting that that the adsorbed ethanol in $[\text{Ni}_{1.5}(\text{4,4}'\text{-bipy})_{1.5}(\text{H}_3\text{L})]\cdot[\text{C}_2\text{H}_5\text{OH}]_{x=0.36-1.1}$ is strongly retained in a relatively stable framework structure over the temperature range studied.

In order to establish the retention of ethanol unequivocally, the desorption kinetics were studied. A typical desorption kinetic profile on the plateau is shown in Figure 5b and other kinetic profiles with fitting to SE and CBRD models are shown in Supporting Information, Figures S12-S15. Figure 5b shows that the kinetic profile for pressure decrement 35-30 mbar at 20°C can be described by a CBRD model and comparison of the profile with the profiles calculated for the barrier resistance and Fickian diffusion components is closer to the LDF model. The SE description of the kinetic profiles shows that the SE exponent (β) values for specific pressures decrements increase with decreasing temperature (see Figure 16b). The higher the value of β the closer the profile is to a LDF model with a surface barrier being the rate

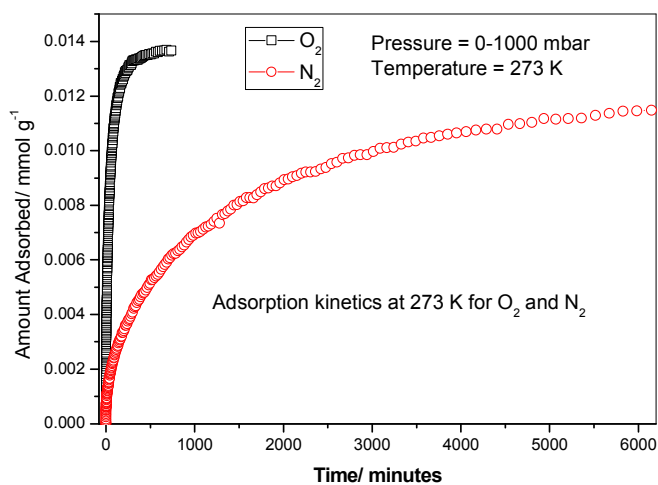
determining process. The desorption kinetic profile for pressure decrement 4-2 mbar at 50°C is shown in Supporting information Figure S15b. It is evident that even at the extremes of temperature and pressure good equilibration is obtained. However, under ultra-high vacuum ethanol is desorbed. This is consistent with diffusion through a surface layer being the main diffusion resistance. A summary of the ethanol desorption kinetic data described using stretched exponential and CBRD models are shown in Supporting Information. Figures S16a and b shows the variation of stretched exponential kinetic parameters as a function of pressure. The desorption kinetics are not markedly influenced by temperature and ethanol loading although there is a relatively small increase in rates of desorption at low pressure. Figures S16c and d shows the variation of CBRD k_B and k_D parameters as a function of pressure, respectively. It is evident that k_B increases with decreasing pressure and increases with increasing temperature. However, the data for different temperatures refer to different ethanol loadings and do not overlap because of the weak dependence of the desorption isotherms on pressure. It is apparent that the effects of temperature, pressure and loading on ethanol desorption are small.

The kinetic parameters for ethanol vapor adsorption can be compared with the corresponding data for water vapor at 20°C. The values of the Fickian Diffusion parameter (k_D) and barrier resistance kinetic parameter (k_B) for ethanol vapor adsorption were in the range $1.9-7.5 \times 10^{-12} \text{ m}^2 \text{ s}^{-1}$ and $1.2 - 4.7 \times 10^{-7} \text{ m s}^{-1}$, respectively. These values have a narrower range than for water vapor ($k_D = 1-10 \times 10^{-12} \text{ m}^2 \text{ s}^{-1}$ and $k_B 4 - 60 \times 10^{-8} \text{ m s}^{-1}$). These distinguishing features reflect

differences in desorption mechanisms and the chemical potential gradient of the respective isotherms.

3.4.3 Kinetic Molecular Sieving for O₂ and N₂

(a)



(b)

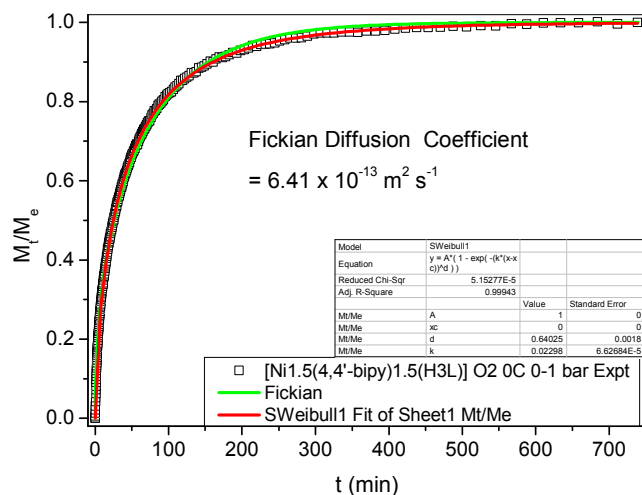


Figure 6. Adsorption Kinetic Profiles for O₂ and N₂ on [Ni_{1.5}(4,4'-bipy)_{1.5}(H₃L)] for pressure increment (0 – 1000 mbar) at 0°C (a) Comparison of O₂ and N₂ and (b) O₂

Kinetic profile with Fickian and Stretched Exponential model descriptions of the experimental data.

The adsorption kinetic profiles for O₂ and N₂ adsorption on [Ni_{1.5}(4,4'-bipy)_{1.5}(H₃L)] for pressure increment 0-1 bar are compared in Figure 6a. It is apparent that N₂ adsorption is much slower than O₂ adsorption. The stretched exponential and Fickian model descriptions for the O₂ data are shown in Figure 6b. It is evident that the kinetic profiles are consistent molecular sieving by diffusion along the pores. The Fickian model is also observed in CMS materials where the kinetic selectivity is homogeneously distributed in the porous structure. However, when the selectivity is achieved by heterogeneous deposition of carbon on a microporous substrate, the kinetics follow an LDF model.^{53, 54} The selective porosity in CMS behaves as though it has a circular rather than slit shaped cross-section.⁵⁵

3.4.4 Carbon Dioxide Adsorption.

The characterization of the porous structure of [Ni_{1.5}(4,4'-bipy)_{1.5}(H₃L)] was carried out using CO₂ adsorption at temperatures in the range 30-75°C, which gave sufficient uptakes and kinetic timescales to allow accurate measurements of thermodynamic and kinetic parameters. The adsorption/desorption isotherms for CO₂ adsorption on [Ni_{1.5}(4,4'-bipy)_{1.5}(H₃L)] do not exhibit significant hysteresis and are shown in Figure 7a and Figure S17. The critical temperature of CO₂ is 31°C. Therefore, the isotherms were analyzed using the virial equation⁵⁶ below

$$\ln(n/p) = A_0 + A_1n + A_2n^2 \quad \text{---} \quad (8)$$

Where p is the pressure, n is the amount absorbed and A_0 , A_1 , A_2 etc are virial

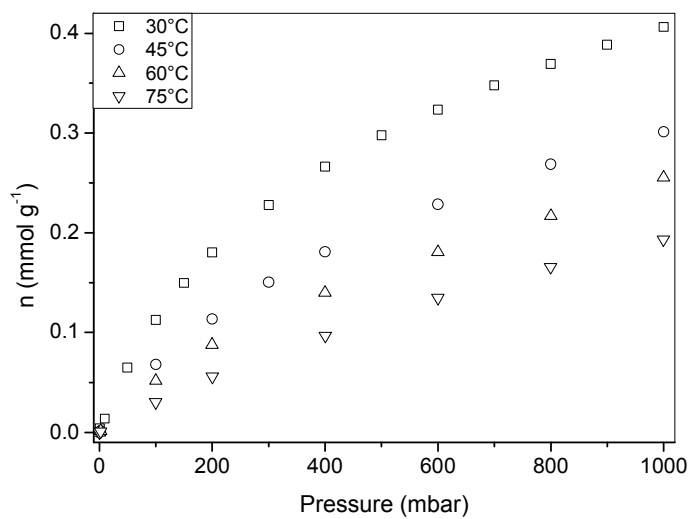
coefficients. The higher virial parameters (A_2 , A_3 etc.---) can be neglected at low surface coverage and a graph of $\ln(n/p)$ versus n can be used to determine A_0 and A_1 ($K_H = \exp(A_0)$, where K_H is the Henry's Law constant). A_0 quantifies the adsorbate-adsorbent interaction, while A_1 describes adsorbate-adsorbate interactions.

The A_1 virial parameter values for CO_2 adsorption varies considerably from -17 to -40 g mol^{-1} ((0 – 40°C)) for NPC-4⁵⁷ to -1902 to -3117 g mol^{-1} (0-40°C) for M'MOF3a⁵⁸ with intermediate values obtained for carbon molecular sieves.⁵⁹ The values obtained for CO_2 adsorption on $[\text{Ni}_{1.5}(\text{4,4' -bipy})_{1.5}(\text{H}_3\text{L})]$ were in the range -2713 to – 3569 g mol^{-1} (30-75°C) (See Supporting Information, Figure S18). These values for A_1 are consistent with the presence of ultramicroporosity and increased adsorbate-adsorbate interactions.

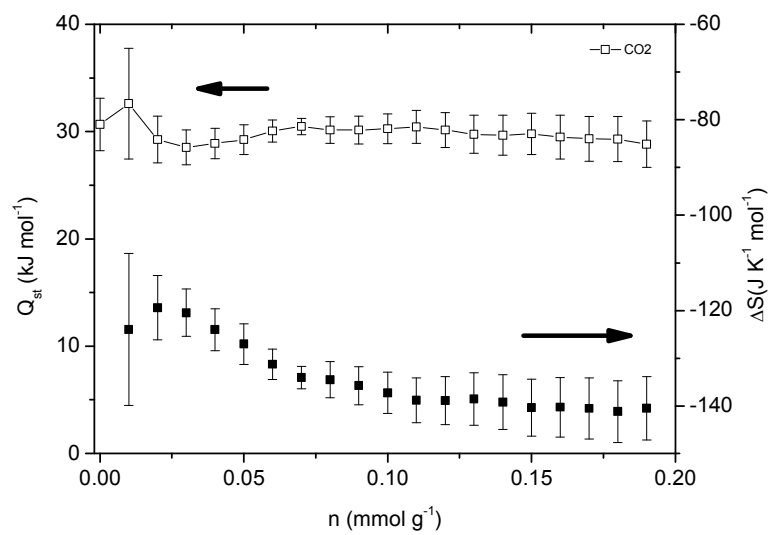
Isosteric Enthalpy of CO_2 Adsorption

The isosteric enthalpy of adsorption at zero surface coverage ($Q_{st,n=0}$), which is a fundamental measure of the CO_2 interaction with the porous structure, was determined from the graph A_0 versus $1/T$ (see Figure S19). The $Q_{st,n=0}$ value was 30.7 ± 2.4 kJ mol^{-1} . The isosteric enthalpies ($Q_{st,n}$) for amounts adsorbed(n) in the range 0.01-0.19 mmol g^{-1} determined using the Clausius-Clapeyron equation were not significantly different from the value at zero surface coverage (Figure 7b).

(a)



(b)

Figure 7. CO₂ Adsorption on [Ni_{1.5}(4,4'-bipy)_{1.5}(H₃L)] (a) isotherms at 30, 45, 60 and

75°C and (b) $Q_{st,n}$ versus amount adsorbed.

The $Q_{st,n}$ values reported in the literature for dehydrated metal phosphonate Ni-STA-12 was 20-35 kJ mol⁻¹⁶⁰ and non-specific physisorption on porous materials are mainly in the range 22-32 kJ mol⁻¹.^{59, 61} There are a few exceptions where specific interactions occur and higher values are reported for CO₂ binding with amine groups⁶² and in ultramicroporous MOFs.⁶³ CO₂ molecules have been shown to interact with the hydrogen-bonded POH--N acid-base pairs in MIL-91(Al) giving a relatively high isosteric enthalpy of adsorption (~40 kJ mol⁻¹).²⁴ The $Q_{st,n}$ values for [Ni_{1.5}(4,4'-bipy)_{1.5}(H₃L)] are within the usual range of values and consistent with physisorption of CO₂. Hence, the unsaturated nickel center has little or no influence on the enthalpy of CO₂ adsorption on [Ni_{1.5}(4,4'-bipy)_{1.5}(H₃L)].

CO₂ Adsorption Kinetics

The adsorption kinetic profiles were measured for each isotherm pressure step and some typical examples are shown in Figure 8 together with the fitting for Fickian, CBRD and stretched exponential kinetic models.

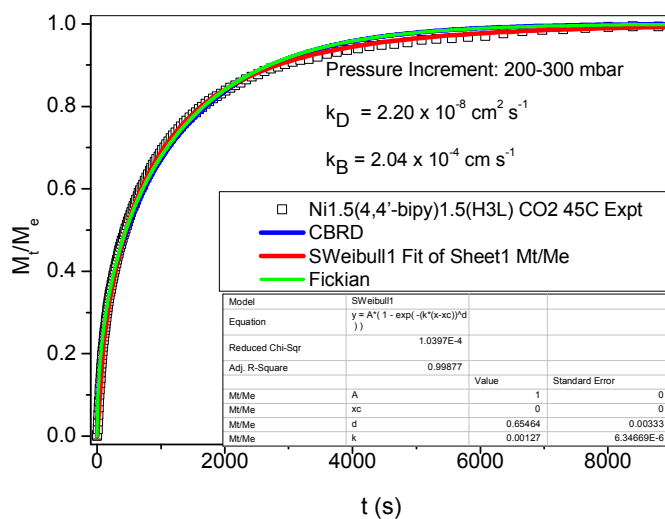


Figure 8. Adsorption Kinetic Profile for CO₂ Adsorption on [Ni_{1.5}(4,4'-bipy)_{1.5}(H₃L)]: Pressure increment 200-300 mbar, 45°C

At low surface coverage the kinetic profiles show that Fickian diffusion along the pores is the main rate determining process (See Figure 8). The k_D values for CO₂ at 30°C are similar to the k_D values at low pressure (0.1-0.2 mbar) for water vapor adsorption at 20°C before the framework structure has fully reformed by water vapor adsorption and ethanol adsorption (0-2 mbar) at 20°C (See Figures 4b, S10a and S12a). The values of the activation energy for diffusion along the pores at specific surface coverages were calculated by linear interpolation of $\ln(k_D)$ and $\ln(k_{SE})$ values, obtained from fitting the experimental data to the CBRD model, for uptakes between adjacent isotherm points. The activation energies were for k_D and k_{SE} , 47.6 ± 9.6 and 47.6 ± 4.0 kJ mol⁻¹ for uptakes at 0.08 mmol g⁻¹, respectively (See Figures S24a and

S24b). These values are higher than the isosteric enthalpy of adsorption indicating that constrictions in the porosity are the main barrier to diffusion in the porous structure. Additional kinetic profiles for CO₂ adsorption are shown in Supporting Information, Figures S20-S23.

3.5 CH₄/CO₂ Selectivity

Kinetic selectivity for gases such as CH₄ and CO₂ is related to differences in the molecular size cross-section, while differences based on the amounts adsorbed are related to the strength of the interaction with surfaces in pores or exclusion from the porous structure based on size/shape. Both kinetic and size exclusion effects may be observed. Previous studies of CO₂/CH₄ selectivity on MOFs have shown that the highest selectivity is at low temperatures.⁶⁴ A comparison of methane and carbon dioxide isotherms at 30°C is shown in Figure 9. It is evident that the uptake of methane is very small. The CO₂/CH₄ selectivity exceeds 1000 at 30°C. The critical temperatures of CO₂ and CH₄ are 31.1 and -82.6°C, respectively. Therefore, CO₂ is subcritical whereas CH₄ is supercritical at 30°C. The CO₂/CH₄ selectivity ratio varies markedly with temperature and this is associated with subcritical pore filling for CO₂ at temperature down to -78°C when CH₄ is supercritical. The CO₂/CH₄ selectivity ratio for [Ni_{1.5}(4,4'-bipy)_{1.5}(H₃L)] is very high compared with other MOFs at 30°C. However the capacity of [Ni_{1.5}(4,4'-bipy)_{1.5}(H₃L)] for CO₂ is smaller. NOTT-202a, which has a partially interpenetrated framework structure has a selectivity of 23.7 at -78°C but only 1.41 at 1 bar 20°C.⁶¹ Breathable framework⁶⁵ and gating mechanisms⁶⁶ with host-CO₂ interaction, which open the framework

structure enhance uptakes and selectivity based on adsorption of pure components. CO₂ adsorption leads to structural change opening the structure whereas CH₄ does not. Studies of co-adsorption of CO₂ and CH₄ mixtures on MIL-53(Cr), show that the breathing of the framework structure is mainly controlled by CO₂ content.⁶⁵ In the case of [Ni_{1.5}(4,4'-bipy)_{1.5}(H₃L)] the high selectivity is attributed to kinetic effects due to the very slow adsorption of the larger CH₄ leading to effective exclusion from the pore structure. It was not possible to determine a selectivity based on Ideal Adsorption Solution Theory (IAST)⁶⁷ because the CH₄ uptake was negligible.

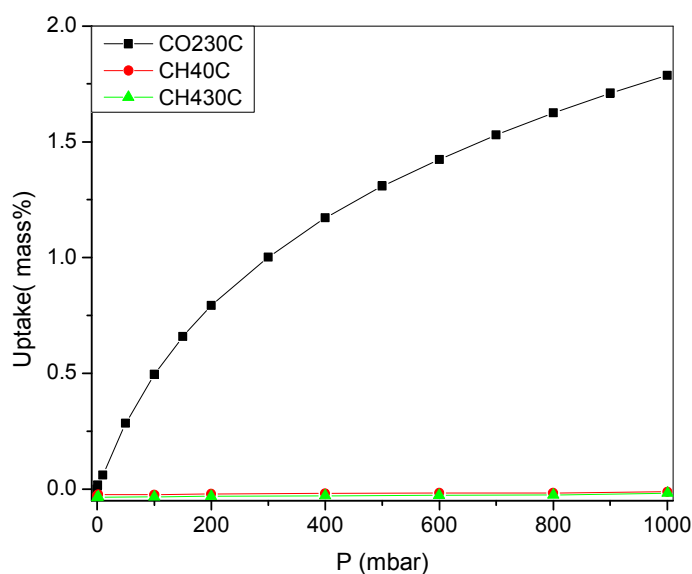


Figure 9. Comparison of isotherms for CO₂ (30°C) and CH₄ (0 and 30°C) adsorption on [Ni_{1.5}(4,4'-bipy)_{1.5}(H₃L)]

4. CONCLUSIONS

[Ni_{1.5}(4,4'-bipy)_{1.5}(H₃L)(H₂O)₃]·[H₂O]₇ was synthesized, the structure determined and gas adsorption characteristics studied. The material readily loses lattice water to form [Ni_{1.5}(4,4'-bipy)_{1.5}(H₃L)(H₂O)₃], which has a porous structure decorated with surface

P-OH acidic groups. The loss of lattice water to give $[\text{Ni}_{1.5}(\text{4,4}'\text{-bipy})_{1.5}(\text{H}_3\text{L})(\text{H}_2\text{O})_3]$ does not change the framework structure significantly. This framework can also lose coordinated water when heated under high vacuum conditions to give $[\text{Ni}_{1.5}(\text{4,4}'\text{-bipy})_{1.5}(\text{H}_3\text{L})]$, which has an ultramicroporous structure with kinetic molecular sieving characteristics for O_2 , N_2 and CO_2 . Adsorption of water vapor on $[\text{Ni}_{1.5}(\text{4,4}'\text{-bipy})_{1.5}(\text{H}_3\text{L})]$ at 20°C leads to the reformation of $[\text{Ni}_{1.5}(\text{4,4}'\text{-bipy})_{1.5}(\text{H}_3\text{L})(\text{H}_2\text{O})_3] \cdot [\text{H}_2\text{O}]_7$ and crystallographic/water vapor pore volumes for the lattice water of $0.185 \text{ cm}^3 \text{ g}^{-1}$. The water vapor desorption kinetic profiles show that lattice water is desorbed at 20°C to give $[\text{Ni}_{1.5}(\text{4,4}'\text{-bipy})_{1.5}(\text{H}_3\text{L})(\text{H}_2\text{O})_3]$. Ethanol has both hydrophobic and hydrophilic characteristics and adsorption on $[\text{Ni}_{1.5}(\text{4,4}'\text{-bipy})_{1.5}(\text{H}_3\text{L})]$ gives approximately linear isotherms with marked adsorption/desorption hysteresis. The stoichiometry at $p/p^0 = 0.97$ was $[\text{Ni}_{1.5}(\text{4,4}'\text{-bipy})_{1.5}(\text{H}_3\text{L})] \cdot [1.11\text{C}_2\text{H}_5\text{OH}]$ this corresponds to pore volume of $0.09 \text{ cm}^3 \text{ g}^{-1}$. Hysteretic adsorption isotherms show that ethanol is strongly retained in the $[\text{Ni}_{1.5}(\text{4,4}'\text{-bipy})_{1.5}(\text{H}_3\text{L})] \cdot [\text{C}_2\text{H}_5\text{OH}]_x$ framework structure.

Adsorption of O_2 , N_2 and CO_2 on $[\text{Ni}_{1.5}(\text{4,4}'\text{-bipy})_{1.5}(\text{H}_3\text{L})]$ shows that the adsorption kinetic profiles follow a Fickian diffusion, combined barrier resistance diffusion or stretched exponential models depending on the amount adsorbed. The material had very high selectivity for kinetic molecular sieving O_2/N_2 . Very high CO_2/CH_4 selectivity is attributed to exclusion of CH_4 from the framework structure. The adsorption kinetics of CO_2 for $[\text{Ni}_{1.5}(\text{4,4}'\text{-bipy})_{1.5}(\text{H}_3\text{L})]$ show that the activation energy for diffusion in the porous structure ($\sim 48 \text{ kJ mol}^{-1}$) was greater than the

enthalpy of adsorption ($\sim 30 \text{ kJ mol}^{-1}$) and this is determined by transport along the pores. This is similar to the trend observed in CMS materials used for air separation. However the rate determining process at low pressure is diffusion along pores in $[\text{Ni}_{1.5}(\text{4,4'}$ -bipy) $_{1.5}(\text{H}_3\text{L})]$ rather than diffusion through a surface barrier as found in CMS materials, where the kinetic selectivity is due to a layer of deposited carbon.

■ ASSOCIATED CONTENT

Supporting Information

Details of synthetic methods and additional characterization data for the ligand are given in Supporting Information, section S1. Additional crystal structure information is provided in Section 2. Scanning electron microscopy, infrared spectra and thermogravimetric analysis are presented in Sections 3, 4 and 5, respectively. Gas adsorption isotherms, virial graphs, isosteric adsorption enthalpy calculations, kinetic profiles and equilibrium selectivity information are presented in section 6. This material is available free of charge via the Internet at <http://pubs.acs.org>. CCDC numbers 1419218 and 1419219 contain the supplementary crystallographic data for this paper. These data can be obtained free of charge from The Cambridge Crystallographic Data Centre via [www.ccdc.cam.ac.uk/data request/cif](http://www.ccdc.cam.ac.uk/data_request/cif).

Author Information

Corresponding Authors

E-mail: mark.thomas@ncl.ac.uk

E-mail: tangsf@qibebt.ac.cn

Notes

The authors declare no competing financial interests.

■ ACKNOWLEDGEMENTS

The authors gratefully acknowledge financial support from the Special Project Fund of "Taishan Scholars" of Shandong Province and Natural Science Foundation of China (Number's. 21473254, 21173246 and 21171173) and 'Hemilabile and Switchable Metal-Organic Frameworks' EPSRC award EP/K005499/1.

■ REFERENCES

1. Sircar, S., Applications of gas separation by adsorption for the future. *Adsorption Science & Technology* **2001**, 19, (5), 347-366.
2. Reid, C. R.; Thomas, K. M., Adsorption Kinetics and Size Exclusion Properties of Probe Molecules for the Selective Porosity in a Carbon Molecular Sieve Used for Air Separation. *J. Phys. Chem. B* **2001**, 105, (43), 10619-10629.
3. Lively, R. P.; Chance, R. R.; Kelley, B. T.; Deckman, H. W.; Drese, J. H.; Jones, C. W.; Koros, W. J., Hollow Fiber Adsorbents for CO₂ Removal from Flue Gas. *Industrial & Engineering Chemistry Research* **2009**, 48, (15), 7314-7324.
4. Bhowan, A. S.; Freeman, B. C., Analysis and Status of Post-Combustion Carbon Dioxide Capture Technologies. *Environmental Science & Technology* **2011**, 45, (20), 8624-8632.
5. Foster, K. L.; Fuerman, R. G.; Economy, J.; Larson, S. M.; Rood, M. J., Adsorption characteristics of trace volatile organic-compounds in gas streams onto activated carbon-fibers. *Chemistry of Materials* **1992**, 4, (5), 1068-1073.
6. Ruhl, M. J., Recover VOCs via Adsorption on Activated Carbon. *Chem. Eng. Prog.* **1993**, 89 (7), 37-41
7. Bhandari, D. A.; Bessho, N.; Koros, W. J., Hollow Fiber Sorbents for Desulfurization of Natural Gas. *Industrial & Engineering Chemistry Research* **2010**, 49, (23), 12038-12050.
8. Kurmoo, M., Magnetic metal-organic frameworks. *Chemical Society Reviews* **2009**, 38, (5), 1353-1379.
9. Zeng, Y. F.; Hu, X.; Liu, F. C.; Bu, X. H., Azido-mediated systems showing different magnetic behaviors. *Chemical Society Reviews* **2009**, 38, (2), 469-480.
10. Allendorf, M. D.; Bauer, C. A.; Bhakta, R. K.; Houk, R. J. T., Luminescent metal-organic frameworks. *Chemical Society Reviews* **2009**, 38, (5), 1330-1352.
11. Ma, L. Q.; Abney, C.; Lin, W. B., Enantioselective catalysis with homochiral metal-organic frameworks. *Chemical Society Reviews* **2009**, 38, (5), 1248-1256.
12. Corma, A.; Garcíà, A. H.; Llabre, S. I.; Xamena, F. X., Engineering Metal Organic Frameworks

- for Heterogeneous Catalysis. *Chemical Reviews* **2010**, 110, (8), 4606-4655.
13. Chen, B. L.; Xiang, S. C.; Qian, G. D., Metal-Organic Frameworks with Functional Pores for Recognition of Small Molecules. *Accounts of Chemical Research* **2010**, 43, (8), 1115-1124.
14. Gagnon, K. J.; Perry, H. P.; Clearfield, A., Conventional and Unconventional Metal-Organic Frameworks Based on Phosphonate Ligands: MOFs and UMOFs. *Chemical Reviews* **2012**, 112, (2), 1034-1054.
15. Maeda, K., Metal phosphonate open-framework materials. *Microporous and Mesoporous Materials* **2004**, 73, (1-2), 47-55.
16. Maeda, K.; Kiyozumi, Y.; Mizukami, F., Synthesis of the First Microporous Aluminum Phosphonate with Organic Groups Covalently Bonded to the Skeleton. *Angewandte Chemie-International Edition in English* **1994**, 33, (22), 2335-2337.
17. Maeda, K.; Akimoto, J.; Kiyozumi, Y.; Mizukami, F., Almpo-Alpha - A Novel Open-Framework Aluminum Methylphosphonate With Organo-Lined Unidimensional Channels. *Angewandte Chemie-International Edition* **1995**, 34, (11), 1199-1201.
18. Lebedeau, J.; Payen, C.; Palvadeau, P.; Bujoli, B., Preparation, Structure, and Magnetic-Properties of Copper(II) Phosphonates - Beta-Cu-II(CH₃PO₃), An Original 3-Dimensional Structure with a Channel-Type Arrangement. *Inorganic Chemistry* **1994**, 33, (22), 4885-4890.
19. Maeda, K.; Akimoto, J.; Kiyozumi, Y.; Mizukami, F., Structure of Aluminum Methylphosphonate, Almpo-Beta, with Unidimensional Channels Formed From Ladder-Like Organic-Inorganic Polymer Chains. *Journal of the Chemical Society-Chemical Communications* **1995**, (10), 1033-1034.
20. Soghomonian, V.; Chen, Q.; Zhang, Y. P.; Haushalter, R. C.; Oconnor, C. J.; Tao, C. H.; Zubieta, J., Hydrothermal Syntheses and Structural Characterization of Layered Oxovanadium Phosphonate Solids Incorporating Organic Cations - H₂N(C₄H₈)NH₂ (VO)₄(OH)₄(PO₄)₂, (NH₃C₃H₆)NH(C₂H₄)₂NH(C₃H₆NH₃) (VO)₅(OH)₂(PO₄)₄ CENTER-DOT-2H₂O, HN(C₂H₄)₃NH₂ (VO)₈(HPO₄)₃(PO₄)₄(OH)₂ CENTER-DOT-2H₂O, and HN(C₂H₄)₃NH (VO)₃(OH)₂(PO₄)₂. *Inorganic Chemistry* **1995**, 34, (13), 3509-3519.
21. Groves, J. A.; Miller, S. R.; Warrender, S. J.; Mellot-Draznieks, C.; Lightfoot, P.; Wright, P. A., The first route to large pore metal phosphonates. *Chemical Communications* **2006**, (31), 3305-3307.
22. Wharmby, M. T.; Pearce, G. M.; Mowat, J. P. S.; Griffin, J. M.; Ashbrook, S. E.; Wright, P. A.; Schilling, L. H.; Lieb, A.; Stock, N.; Chavan, S.; Bordiga, S.; Garcia, E.; Pirngruber, G. D.; Vreeke, M.; Gora, L., Synthesis and crystal chemistry of the STA-12 family of metal N,N'-piperazinebis(methylenephosphonate)s and applications of STA-12(Ni) in the separation of gases. *Microporous and Mesoporous Materials* **2012**, 157, 3-17.
23. Serre, C.; Groves, J. A.; Lightfoot, P.; Slawin, A. M. Z.; Wright, P. A.; Stock, N.; Bein, T.; Haouas, M.; Taulelle, F.; Ferey, G., Synthesis, structure and properties of related microporous N,N'-piperazinebismethylenephosphonates of aluminum and titanium. *Chemistry of Materials* **2006**, 18, (6), 1451-1457.
24. Llewellyn, P. L.; Garcia-Rates, M.; Gaberova, L.; Miller, S. R.; Devic, T.; Lavalley, J. C.; Bourrelly, S.; Bloch, E.; Filinchuk, Y.; Wright, P. A.; Serre, C.; Vimont, A.; Maurin, G., Structural Origin of Unusual CO₂ Adsorption Behavior of a Small-Pore Aluminum Bisphosphonate MOF. *Journal of Physical Chemistry C* **2015**, 119, (8), 4208-4216.
25. Cao, G.; Lee, H.; Lynch, V. M.; Mallouk, T. E., Structural Studies of Some New Lamellar Magnesium, Manganese and Calcium Phosphonates. *Solid State Ionics* **1988**, 26, (2), 63-69.

26. Poojary, D. M.; Grohol, D.; Clearfield, A., Synthesis and X-ray Powder Structure of a Novel Porous Uranyl Phenylphosphonate containing Unidimensional Channels Flanked by Hydrophobic Regions. *Angewandte Chemie-International Edition in English* **1995**, *34*, (13-14), 1508-1510.
27. Poojary, D. M.; Cabeza, A.; Aranda, M. A. G.; Bruque, S.; Clearfield, A., Structure determination of a complex tubular uranyl phenylphosphonate, $(\text{UO}_2)_3(\text{HO}_3\text{PC}_6\text{H}_5)_2(\text{O}_3\text{PC}_6\text{H}_5)_2 \cdot \text{H}_2\text{O}$, from conventional X-ray powder diffraction data. *Inorganic Chemistry* **1996**, *35*, (6), 1468-1473.
28. Grohol, D.; Clearfield, A., Solid-state water-catalyzed transformation at room temperature of a nonluminescent linear-chain uranyl phenylphosphonate into a luminescent one. *Journal of the American Chemical Society* **1997**, *119*, (20), 4662-4668.
29. Aranda, M. A. G.; Cabeza, A.; Bruque, S.; Poojary, D. M.; Clearfield, A., Polymorphism and phase transition in nanotubular uranyl phenylphosphonate: $(\text{UO}_2)_3(\text{HO}_3\text{PC}_6\text{H}_5)_2(\text{O}_3\text{PC}_6\text{H}_5)_2 \cdot \text{H}_2\text{O}$. *Inorganic Chemistry* **1998**, *37*, (8), 1827-1832.
30. Taylor, J. M.; Vaidyanathan, R.; Iremonger, S. S.; Shimizu, G. K. H., Enhancing Water Stability of Metal-Organic Frameworks via Phosphonate Monoester Linkers. *Journal of the American Chemical Society* **2012**, *134*, (35), 14338-40.
31. Kim, S.; Dawson, K. W.; Gelfand, B. S.; Taylor, J. M.; Shimizu, G. K. H., Enhancing Proton Conduction in a Metal-Organic Framework by Isomorphous Ligand Replacement. *Journal of the American Chemical Society* **2013**, *135*, (3), 963-966.
32. Colodrero, R. M. P.; Olivera-Pastor, P.; Losilla, E. R.; Hernandez-Alonso, D.; Aranda, M. A. G.; Leon-Reina, L.; Rius, J.; Demadis, K. D.; Moreau, B.; Villemin, D.; Palomino, M.; Rey, F.; Cabeza, A., High Proton Conductivity in a Flexible, Cross-Linked, Ultramicroporous Magnesium Tetrakisphosphate Hybrid Framework. *Inorganic Chemistry* **2012**, *51*, (14), 7689-7698.
33. Bazaga-Garcia, M.; Colodrero, R. M. P.; Papadaki, M.; Garczarek, P.; Zon, J.; Olivera-Pastor, P.; Losilla, E. R.; Leon-Reina, L.; Aranda, M. A. G.; Choquesillo-Lazarte, D.; Demadis, K. D.; Cabeza, A., Guest Molecule-Responsive Functional Calcium Phosphonate Frameworks for Tuned Proton Conductivity. *Journal of the American Chemical Society* **2014**, *136*, (15), 5731-5739.
34. Taylor, J. M.; Dawson, K. W.; Shimizu, G. K. H., A Water-Stable Metal-Organic Framework with Highly Acidic Pores for Proton-Conducting Applications. *Journal of the American Chemical Society* **2013**, *135*, (4), 1193-1196.
35. Fawcett, J.; Platt, A. W. G.; Vickers, S., Synthesis of tripodal tris-phosphonate ligands and the structure of the dimeric complex, $\text{Ce}(\text{NO}_3)_3\{(\text{EtO})_2\text{P}(\text{O})\text{CH}_2\}_3\text{C}_6\text{Me}_3$ (2). *Polyhedron* **2003**, *22*, (11), 1431-1435.
36. Murugavel, R.; Singh, M. P., One, two, and three methylene phosphonic acid groups ($-\text{CH}_2\text{PO}_3\text{H}_2$) on a mesitylene ring: synthesis, characterization and aspects of supramolecular aggregation. *New Journal of Chemistry* **2010**, *34*, (9), 1846-1854.
37. *SAINT, Version 6.45*. Bruker Analytical X-ray Systems Inc.: 2003.
38. Sheldrick, G. M. *SADABS*, SADABS, Bruker Analytical X-ray Systems Inc.: Madison, WI, US: 2003.
39. Sheldrick, G. M., *SHELXS-97, Program for Crystal Structure Solution and Refinement*. University of Göttingen: 1997; p SHELXS-97, Program for Crystal Structure Solution and Refinement.
40. Sheldrick, G. M. *SHELXTL, Crystallographic Software Package 5.1*; Bruker Analytical X-ray Systems Inc.: Madison, WI, US: 1998.
41. Macrae, C. F.; Edgington, P. R.; McCabe, P.; Pidcock, E.; Shields, G. P.; Taylor, R.; Towler, M.;

- van De Streek, J., Mercury: visualization and analysis of crystal structures. *Journal of Applied Crystallography* **2006**, 39, 453-457.
42. Yaws, C. L.; Narasimhan, P. K.; Gabbula, C., *Yaws' Handbook of Antoine Coefficients for Vapor Pressure (2nd Electronic Edition)*, (pp:19,26) Knovel.
Online version available at:
http://knovel.com/web/portal/browse/display?_EXT_KNOVEL_DISPLAY_bookid=1183&VerticalID=0. 2010.
43. Klafter, J.; Shlesinger, M. F., On the Relationship Among 3 Theories of Relaxation in Disordered-Systems. *Proceedings of the National Academy of Sciences of the United States of America* **1986**, 83, (4), 848-851.
44. Li, L. J.; Bell, J. G.; Tang, S. F.; Lv, X. X.; Wang, C.; Xing, Y. L.; Zhao, X. B.; Thomas, K. M., Gas Storage and Diffusion through Nanocages and Windows in Porous Metal-Organic Framework Cu-2(2,3,5,6-tetramethylbenzene-1,4-diisophthalate)(H₂O)(2). *Chemistry of Materials* **2014**, 26, (16), 4679-4695.
45. Fletcher, A. J.; Yuzak, Y.; Thomas, K. M., Adsorption and desorption kinetics for hydrophilic and hydrophobic vapors on activated carbon. *Carbon* **2006**, 44, (5), 989-1004.
46. Anderssen, R. S.; Edwards, M. P.; Husain, S. A.; Loy, R. J., Sums of Exponentials Approximations for the Kohlrausch Function. *19th International Congress on Modelling and Simulation (Modsim2011)* **2011**, 263-269.
47. Crank, J., *The mathematics of diffusion*. 2nd ed.; Clarendon Press: Oxford, 1975.
48. Loughlin, K. F.; Hassan, M. M.; Fatehi, A. I.; Zahur, M., Rate and equilibrium sorption parameters for nitrogen and methane on carbon molecular sieve. *Gas Separation and Purification* **1993**, 7, (4), 264-273.
49. Fletcher, A. J.; Thomas, K. M., Compensation effect for the kinetics of adsorption/desorption of gases/vapors on microporous carbon materials. *Langmuir* **2000**, 16, (15), 6253-6266.
50. Fletcher, A. J.; Cussen, E. J.; Prior, T. J.; Rosseinsky, M. J.; Kepert, C. J.; Thomas, K. M., Adsorption dynamics of gases and vapors on the nanoporous metal organic framework material Ni-2(4,4'-bipyridine)(3)(NO₃)(4): Guest modification of host sorption behavior. *Journal of the American Chemical Society* **2001**, 123, (41), 10001-10011.
51. Fletcher, A. J.; Cussen, E. J.; Bradshaw, D.; Rosseinsky, M. J.; Thomas, K. M., Adsorption of gases and vapors on nanoporous Ni-2(4,4'-bipyridine)(3)(NO₃)(4) metal-organic framework materials templated with methanol and ethanol: Structural effects in adsorption kinetics. *Journal of the American Chemical Society* **2004**, 126, (31), 9750-9759.
52. *CRC Handbook of Chemistry and Physics*. 74th ed.; The Chemical Rubber Co.: Boca Raton, Florida, 1993.
53. Chagger, H. K.; Ndaji, F. E.; Sykes, M. L.; Thomas, K. M., Kinetics of Adsorption and Diffusional Characteristics of Carbon Molecular Sieves. *Carbon* **1995**, 33, (10), 1405-1411.
54. Okoye, I. P.; Benham, M.; Thomas, K. M., Adsorption of gases and vapors on carbon molecular sieves. *Langmuir* **1997**, 13, (15), 4054-4059.
55. Reid, C. R.; Thomas, K. M., Adsorption kinetics and size exclusion properties of probe molecules for the selective porosity in a carbon molecular sieve used for air separation. *Journal of Physical Chemistry B* **2001**, 105, (43), 10619-10629.
56. Cole, J. H.; Everett, D. H.; Marshall, C. T.; Paniego, A. R.; Powl, J. C.; Rodriguez-Reinoso, F., Thermodynamics of high temperature adsorption of some permanent gases by porous carbons *J.*

Chem. Soc. Faraday Trans. **1974**, 70, 2154-2169.

57. Li, L.; Bell, J. G.; Tang, S.; Lv, X.; Wang, C.; Xing, Y.; Zhao, X.; Thomas, K. M., Gas Storage and Diffusion through Nanocages and Windows in Porous Metal-Organic Framework Cu-2(2,3,5,6-tetramethylbenzene-1,4-diisophthalate)(H₂O)(2). *Chemistry of Materials* **2014**, 26, (16), 4679-4695.
58. Xiang, S. C.; Zhang, Z. J.; Zhao, C. G.; Hong, K. L.; Zhao, X. B.; Ding, D. R.; Xie, M. H.; Wu, C. D.; Das, M. C.; Gill, R.; Thomas, K. M.; Chen, B. L., Rationally tuned micropores within enantiopure metal-organic frameworks for highly selective separation of acetylene and ethylene. *Nature Communications* **2011**, 2, 204.
59. Reid, C. R.; Thomas, K. M., Adsorption of gases on a carbon molecular sieve used for air separation: Linear adsorptives as probes for kinetic selectivity. *Langmuir* **1999**, 15, (9), 3206-3218.
60. Miller, S. R.; Pearce, G. M.; Wright, P. A.; Bonino, F.; Chavan, S.; Bordiga, S.; Margiolaki, I.; Guillou, N.; Feerey, G.; Bourrelly, S.; Llewellyn, P. L., Structural Transformations and Adsorption of Fuel-Related Gases of a Structurally Responsive Nickel Phosphonate Metal-Organic Framework, Ni-STA-12. *Journal of the American Chemical Society* **2008**, 130, (47), 15967-15981.
61. Yang, S.; Lin, X.; Lewis, W.; Suyetin, M.; Bichoutskaia, E.; Parker, J. E.; Tang, C. C.; Allan, D. R.; Rizkallah, P. J.; Hubberstey, P.; Champness, N. R.; Thomas, K. M.; Blake, A. J.; Schroeder, M., A partially interpenetrated metal-organic framework for selective hysteretic sorption of carbon dioxide. *Nature Materials* **2012**, 11, (8), 710-716.
62. Vaidhyanathan, R.; Iremonger, S. S.; Shimizu, G. K. H.; Boyd, P. G.; Alavi, S.; Woo, T. K., Direct Observation and Quantification of CO₂ Binding Within an Amine-Functionalized Nanoporous Solid. *Science* **2010**, 330, (6004), 650-653.
63. Nugent, P.; Belmabkhout, Y.; Burd, S. D.; Cairns, A. J.; Luebke, R.; Forrest, K.; Pham, T.; Ma, S. Q.; Space, B.; Wojtas, L.; Eddaoudi, M.; Zaworotko, M. J., Porous materials with optimal adsorption thermodynamics and kinetics for CO₂ separation. *Nature* **2013**, 495, (7439), 80-84.
64. Li, J. R.; Sculley, J.; Zhou, H. C., Metal-Organic Frameworks for Separations. *Chemical Reviews* **2012**, 112, (2), 869-932.
65. Hamon, L.; Llewellyn, P. L.; Devic, T.; Ghoufi, A.; Clet, G.; Guillerm, V.; Pirngruber, G. D.; Maurin, G.; Serre, C.; Driver, G.; van Beek, W.; Jolimaitre, E.; Vimont, A.; Daturi, M.; Ferey, G., Co-adsorption and separation of CO₂-CH₄ mixtures in the highly flexible MIL-53(Cr) MOF. *J Am Chem Soc* **2009**, 131, (47), 17490-9.
66. Wang, C.; Li, L.; Bell, J. G.; Lv, X.; Tang, S.; Zhao, X.; Thomas, K. M., Hysteretic Gas and Vapor Sorption in Flexible Interpenetrated Lanthanide-Based Metal-Organic Frameworks with Coordinated Molecular Gating via Reversible Single-Crystal-to-Single-Crystal Transformation for Enhanced Selectivity. *Chemistry of Materials* **2015**, 27, (5), 1502-1516.
67. Myers, A. L.; Prausnitz, J. M., Thermodynamics of mixed-gas adsorption. *Aiche Journal* **1965**, 11, (1), 121-127.

TOC Graphic